Chapter 5

Separation of Charged Particles from Their Turbulent Magnetic Field Lines

In this chapter we explore the separation of charged particles and magnetic field lines in two cases which are Guassian 2D Field + slab turbulence and 2D+slab turbulence. For simple case, we release the particles at various distances from the center of Guassian island and then study behavior for each case. For 2D + slab turbulence, we vary particle energy, 2D fraction, initial pitch angle, and the fluctuation strength in order to see the effect of separation.

5.1 Separation of Charged Particles and Field Lines in Guassian 2D Field + Slab Turbulence

The 1000 charged particles are released at random initial pitch angles on various distances from the center of the 2D Gaussian island (r_0) as $0.1\lambda, 0.3\lambda, 0.5\lambda, 0.7\lambda,$ and 0.9λ (Wikee 2013). For Gaussian function of potential function, we set the width of the Gaussian σ as 0.5λ . We define $b_{2D}^{max}/B_0 = 1.0$ and $(b_{2D}^{max}/\delta b_{slab})^2 = 20$ that means the 2D flux tube is very strong compared with slab turbulence. The test particles are designed to represent protons that have energy 100 MeV. In our simulations, all units of lengths are scaled with λ and the unit of the time is scaled by λ/c. Figure 5.1 shows the example of the trajectory of the test charged particle and magnetic field line.

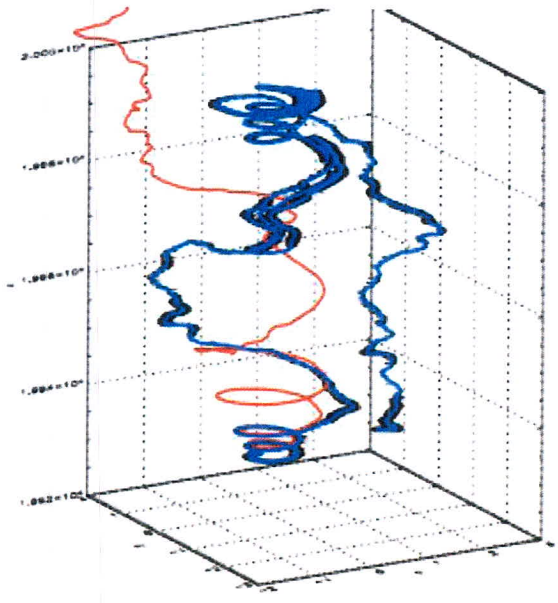

Figure 5.1 Example of the trajectory of a charged particle in our model; red line demonstrates trajectory of magnetic field line, black line and blue line demonstrate trajectories of charged particle and its guiding centers, respectively.

In our work, the simulation results for 1,000 particles show that the separation behaviors between the charged particles and the corresponding field lines can be divided into several regimes as we can see in Figure 5.2. We can explain the mechanism of separation in each regime by relating to the structure of the 2D Gaussian and slab turbulent magnetic field.

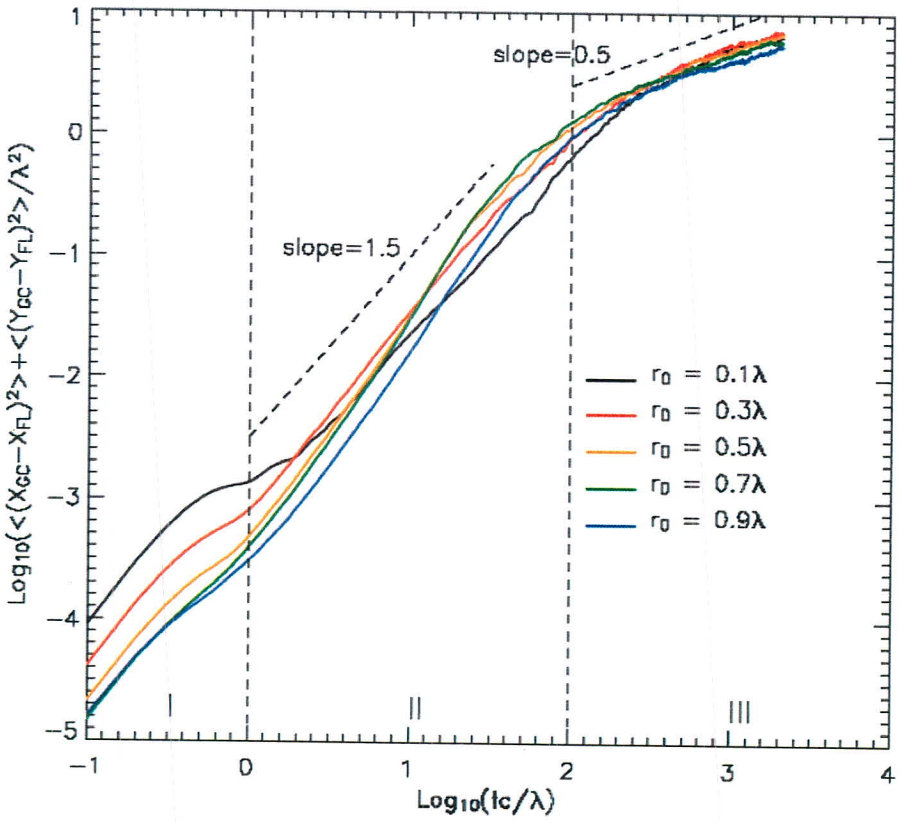

Figure 5.2 The results of the separation of charged particles and their corresponding field lines in the log-log scale.

I. At the initial times (when $tc/\lambda < 1$)

We found that the separation of the charged particles in initial time which are started at the radius of 0.1λ is highest one following by the ones started at 0.3λ and 0.5λ , respectively. For the particles started at 0.7λ and 0.9λ, the separations are very close to each other and lower than the particles started $r_0 = 0.5\lambda$. It seems that the separation of charged particles during this time depend on the structure of 2D field which can be explained by the radius of curvature of the magnetic field and the gradient of magnetic field. The positions of 0.1λ from center of Gaussian function have the lower radius of curvature of the magnetic field lines than the radii as 0.3λ, 0.5λ, 0.7λ and 0.9λ. The curvature is larger when the distance is far from the center. For the gradient of magnetic field, we can see from the profile of the intensity of 2D Gaussian flux can

be seen in Figure 5.3. The gradient depends on the radius from the center of Gaussian 2D field. The maximum of 2D magnetic field is at the width of Gaussian function (σ) and the decrease when the radius towards to the center as well as when they go outside. Next, we compute the effect of curvature and gradient drifts due to 2D Gaussian field in order to explain the results during the beginning time. In general, the drift velocity of guiding center due to the gradient of the magnetic field is represented by

$$\vec{v}_G = \frac{v_\perp^2}{2\omega_c}\frac{\vec{B}\times\nabla\vec{B}}{B^2} \tag{5.1}$$

while the curvature drift is

$$\vec{v}_c = \frac{\gamma m v_{//}^2}{qB^2}\frac{\vec{R}_c\times\vec{B}}{R_c^2}. \tag{5.2}$$

Then we plug in the pure Gaussian 2D magnetic field including mean field into equations (5.1) and (5.2) and compute the drift velocity. Then we can find that the magnitude of drift velocity of the guiding center due to the gradient and the curvature drift of the magnetic field are

$$\|\langle\vec{v}_G\rangle\| = \frac{\gamma m v^2}{3q\sigma^2 R_c}\frac{b^{2D}}{B^2}|\sigma^2 - R_c^2| \tag{5.3}$$

$$\|\vec{v}_C\| = \frac{\gamma m v^2}{3qR_cB}. \tag{5.4}$$

Then when we consider both effects, the equation for these is

$$\|\langle\vec{v}_G\rangle + \langle\vec{v}_C\rangle\| = \frac{\gamma m v^2}{3qBR_c}\left|\left[\left(\frac{b^{2D}(R_c)}{B\sigma^2}\right)(\sigma^2 - R_c^2) + 1\right]\right|. \tag{5.5}$$

After that, we insert all magnetic field parameters in our simulation into equations (5.3), (5.4), and (5.5) and make a map to see the effect of the drift for each radius from the center of Gaussian. We found that they give the shapes of drift speed like Figure 5.4. From the drift speed profile, we can see that the curvature drift has more effect than the gradient drift and it is dominated at the small radius from the center of the Gaussian function. When we combine these two effects as in equation (5.5), the particles started near the center of the Gaussian have more drift speed due to 2D field. That is why we can see the charged particles have high separation of

the charged particles when they are released at the small radius as shown in Figure 5.2. Moreover, from the profile in Figure 5.4, the effect of the drift for the particles started at $0.7\lambda$and 0.9λ is slightly different which we can also see this effect in Figure 5.2.

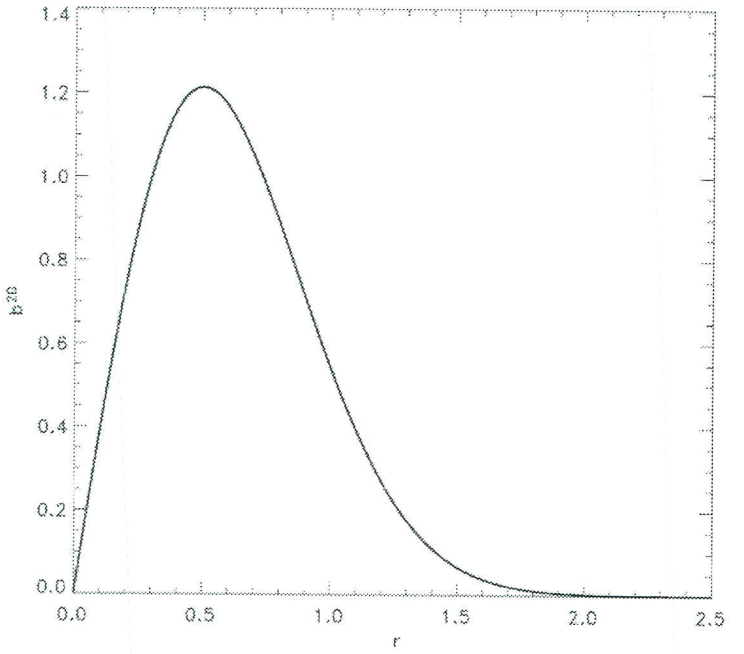

Figure 5.3 The profile of the 2D Gaussian magnetic field along the distance from the center of the flux tube.

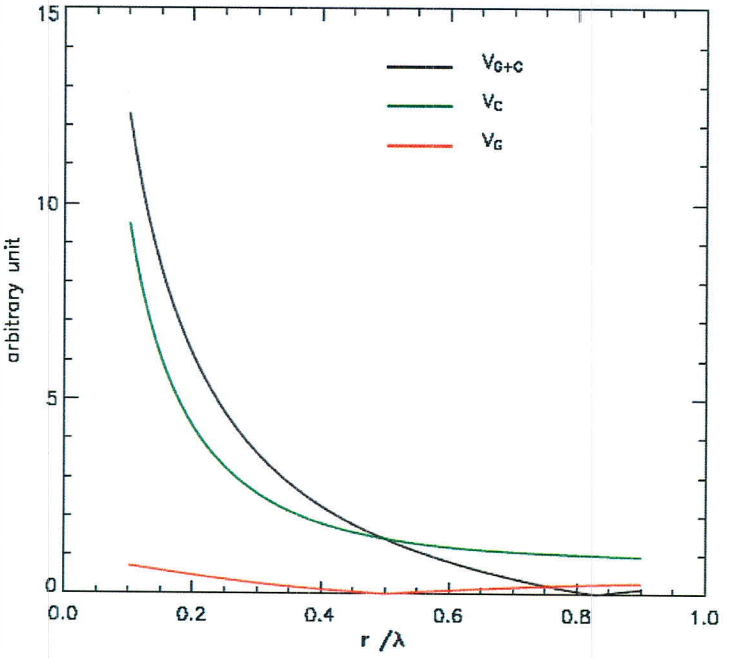

Figure 5.4 Showing shape of drift speed of guiding center due to the gradient of the magnetic field, radius of curvature of the magnetic field line and the summation of the gradient drift and curvature drift in arbitrary units.

II. At intermediate time (when $1 \leq tc/\lambda \leq 100$)

In this regime, the charged particles follow their corresponding field lines for a while and start to escape from the influence of the 2D flux tube. There are interesting features in this regime. The particles started deeper inside the 2D island have lower separation during this time and the particles started outside 2D island have almost the same slope of the separation. The particles start at $r_0 = 0.1\lambda$ and 0.3λ, at inside 2D islands, have lower separation rate than the others as shown in Figure 5.5a). Here, we can recognize the separation rate by the slope of the graph. The particles started deep inside the 2D island slowly drift out from the field lines because both field lines and the charged particles are trapped inside 2D island. For the behaviors of the particles released outside the 2D island such as at $r_0 = 0.5\lambda$, 0.7λ and 0.9λ, they have almost the same separation rate and there is more the separation rate than the particles started at inside 2D island as shown in Figure 5.5b). That is because these particles quickly move outside and are not

trapped due to the strong 2D field. This corresponds with the suppression of field line and particle diffusion when there is a strong 2D magnetic field as found in previous work (Chuychai et al., 2005, 2007; Tooprakai et al., 2007).

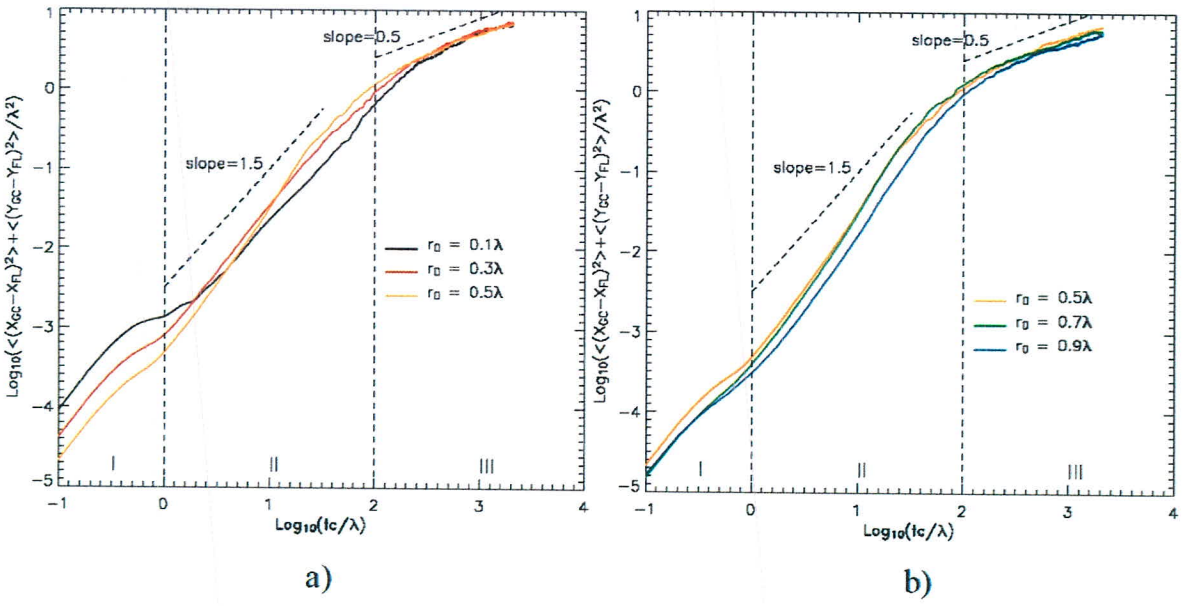

Figure 5.5 Showing the separation of the charged particles at a) inside the 2D island and b) outside the 2D island.

III. At final time (when $tc/\lambda \gg 100$)

From the final range in Figure 5.6, we can see that the charged particles released at radius as 0.1λ, 0.3λ and 0.5λ separate faster than the other radii. It seems the separation is related to the radius of releasing the charged particles. If the charged particles are released inside the center of Gaussian function, they separate from their initial field lines more than the other positions. In this range, the transition of the charged particles and their corresponding magnetic field lines are uncorrelated. Note that the corresponding length scale of the uncorrelation between particles and field lines is in the order of coherence length scale (λ) which, within this length scale, the slab field are still correlated. The charged particles are mainly influenced by slab turbulence and undergo subdiffusive as we can see from the slope = 0.5 in Figure 452. We normally find subdiffusive process when charged particles transport in pure slab magnetic field (Tooprakai et al., 2007).

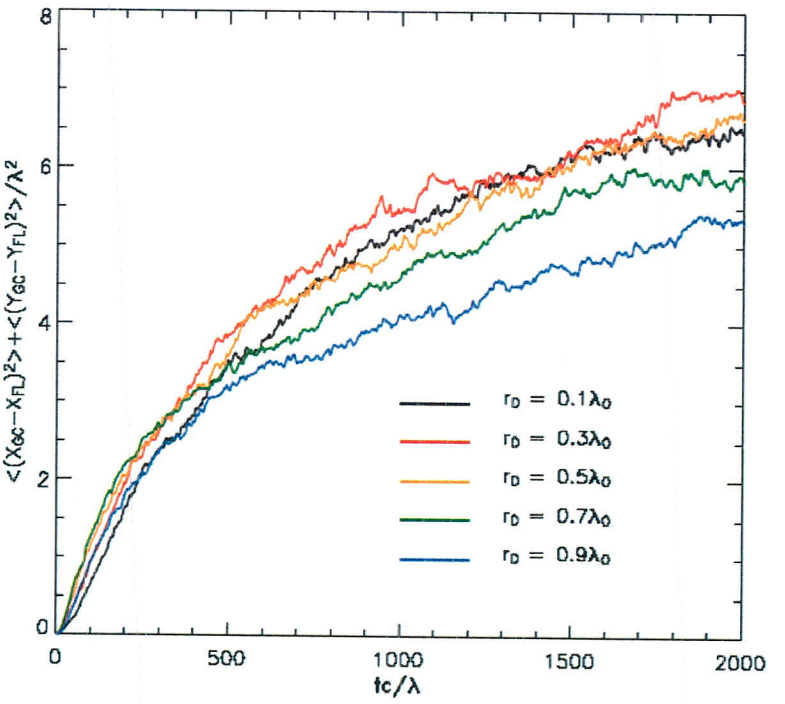

Figure 5.6 The mean squared perpendicular displacement and time in the final range.

From the results in this section, the separation of the charged particles are related with the distance from the center of the Gaussian flux tube (r_0) and where they experience the different structure of the magnetic field. When the charged particles are released at low curvature of the magnetic field line, the separation is more than the others at the initial times. In our results, we show that the separation at the beginning depend on the gradient and curvature drift due to the 2D field. Then, in intermediate time, they slowly drift to outside the 2D flux tube. The sharp gradient of 2D field can be distinct behavior of the particles inside and outside the island in this regime. It corresponds with the suppressed diffusive regime in the previous work (Chuychai et al., 2007; Tooprakai et al., 2007). In addition, for final time the separation of the charged particles is uncorrected with the starting point to release the charged particles. The separation of the charged particles depends on distance from the center of the Gaussian function and becomes subdiffusive, the charged particles are released at outside of 2D Gaussian field ($r_0 = 0.7\lambda$ and 0.9λ), the separation is lower than the others radius. Finally, this work can help us to understand

more about the relation of the separation between guiding centers of charged particles and magnetic field lines. In the next section, we present the effect of separation in 2D+slab turbulence.

5.2 Separation of Charged Particles and their field lines in 2D+Slab tubuelence

Here we release the charged particles in 2D+slab turbulence inn various cases. We also trace the sample of charged particles and their magnetic field line which are started at the initial GC in pure slab and 2D+slab turbulence cases as shown in Figure 5.7

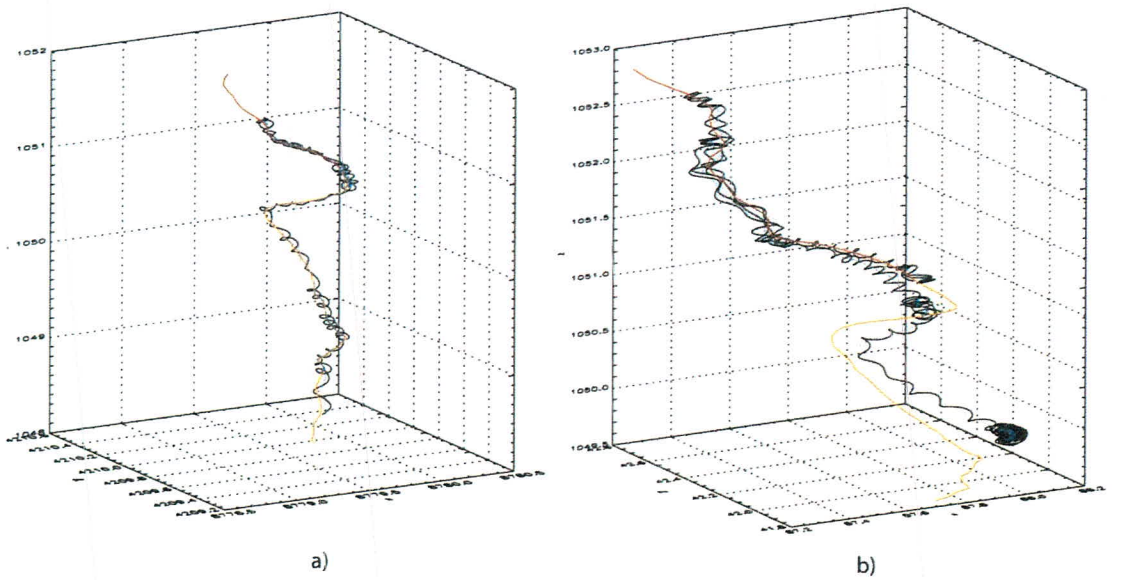

Figure 5.7 Examples of 20 MeV particle trajectories (BLACK lines), their guiding centers (BLUE dots), and their initial field lines (RED lines) in a) pure slab turbulence and b) 10% 2D+ 90% slab turbulence. Note that in our simulations the time scale is in units of λ/c and the length scale is in units of λ, where λ is the slab coherence scale and c is the speed of light.

We can see that the particle in pure slab case ties along the field lines while the particles from 2D+slab turbulence follow the field line at the beginning and then deviate from its field lines at the later time. Figure 5.8 shows the statistics when we release 1,000 particles and compute the mean squared of separation between particle's GCs and their field lines in both pure slab and 2D+slab turbulence. For the pure slab case, the results show that the particles in pure slab turbulence have very little

separation between particle trajectories and their field lines. The particles stick with their initial field lines. This is consistent with the theorem of Jokipii et al. (1993) and Jones et al. (1998). This effect happens when we reduce the dimensionality of the magnetic field. Despite from the particles in 2D+slab case, they diffuse along the time.

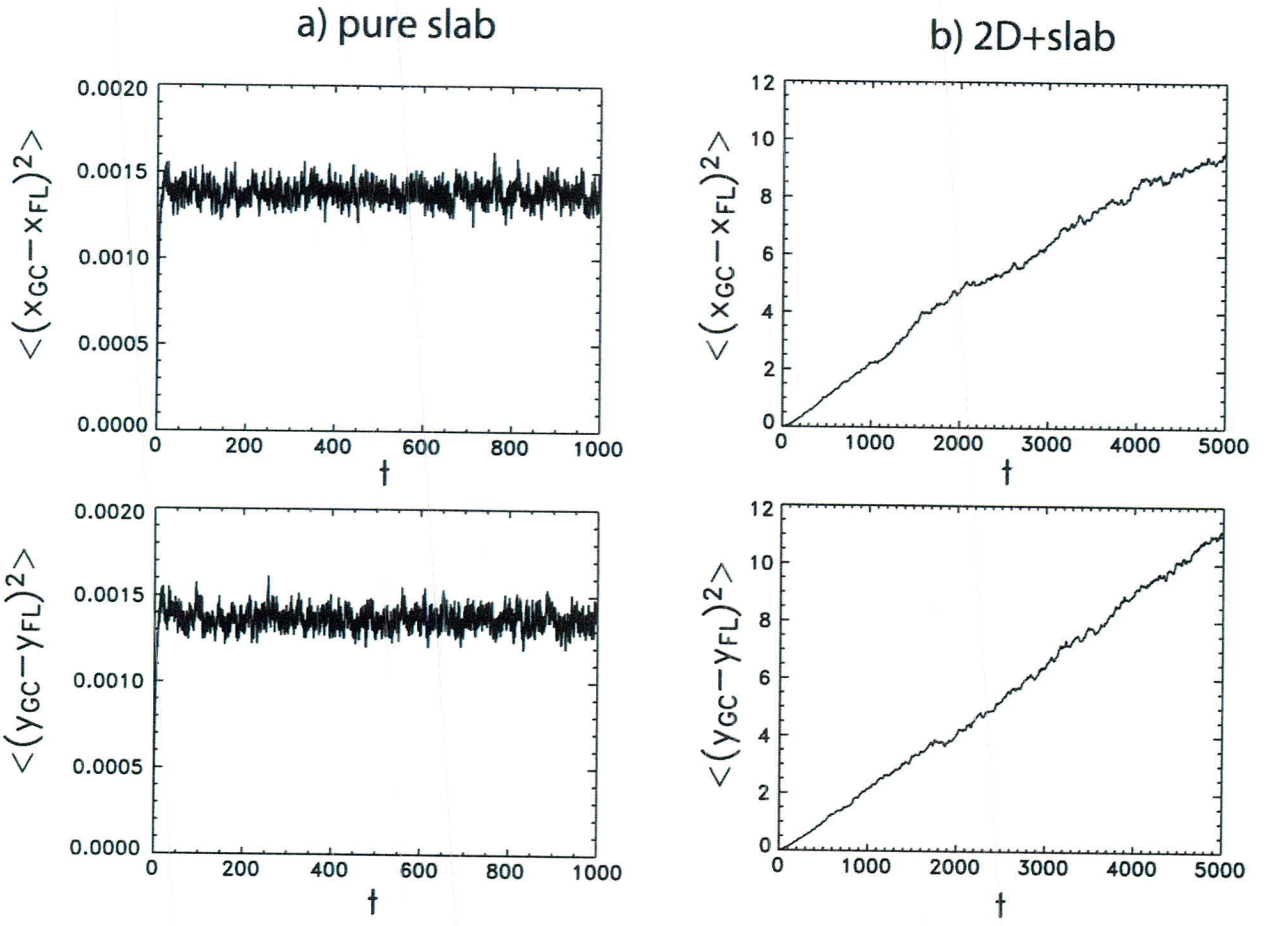

Figure 5.8 The results from the simulations of 100 MeV protons in a) pure slab and b) 2D+slab turbulence. The statistics in the plots show the spreading of particles from field lines as a function of time.

After that we perform the simulations for 1,000 charged particles in various cases to see the effect the many parameters to the separation such as particle energy, initial pitch angle, 2D fraction, and magnetic field strength.

Figure 5.9 shows how different particle energy responds to the separation. From the results we can see that low energy particles have lower separation than high energy particles. At intermediate time, very low energy particles stay or tie to the magnetic field before they leave the field lines as we can see the flat shape of the plot in Figure 5.9 for 10 keV and 1 MeV particles.

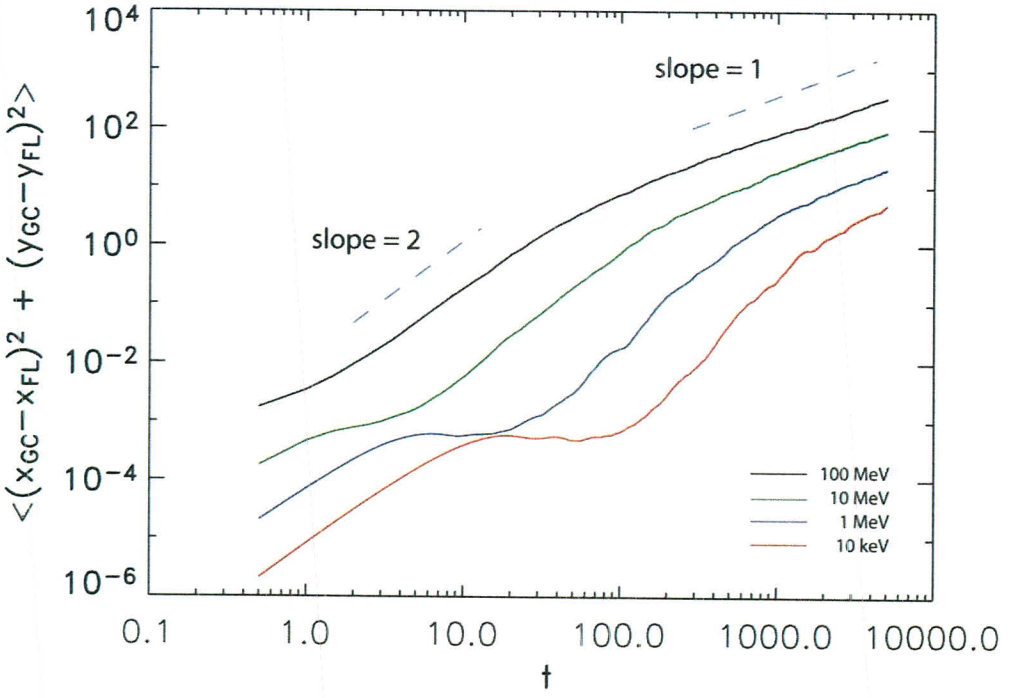

Figure 5.9 The results of the separation of charged particles and their corresponding field lines when we vary particle energy.

Next, we vary the initial pitch angle of the charged particles. The pitch angle is defined by the angle between velocity of particle and magnetic field. From the results in Figure 5.10, we found that the particles moving perpendicular to the magnetic field give more separation than the ones start in the direction parallel to the magnetic field. For long time limit, the separation reaches the same rate for all initial pitch angles.

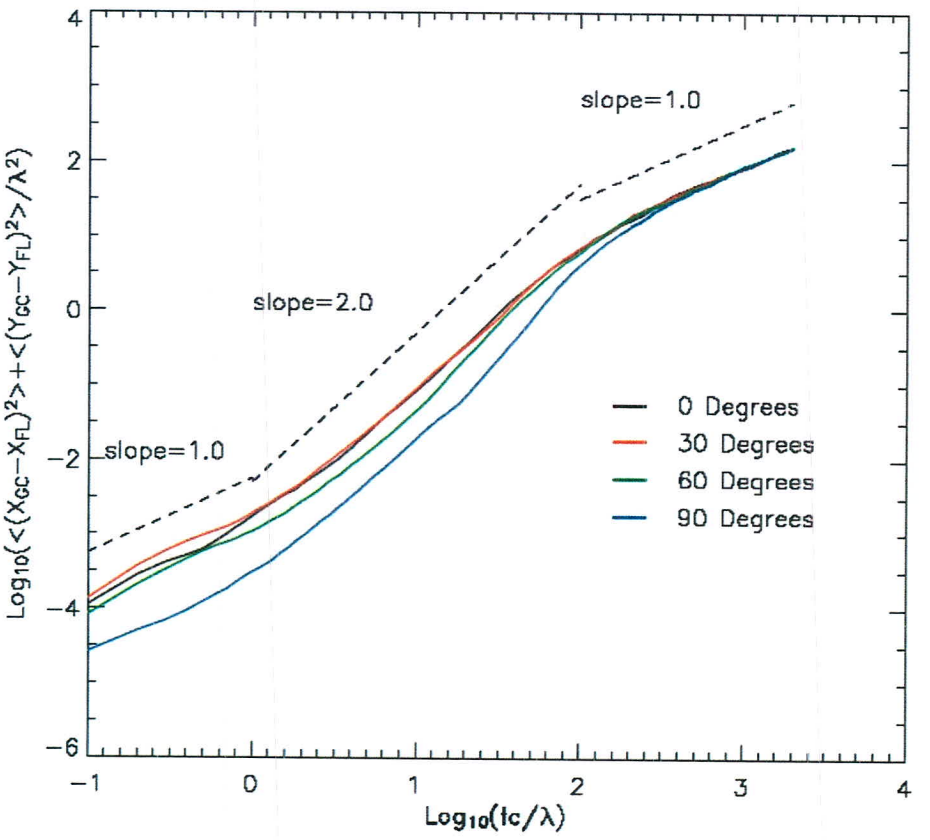

Figure 5.10 The results of the separation of charged particles and their corresponding field lines when we vary initial pitch angles.

We also vary 2D fraction to 10%, 20%, 50%, and 80%. We found that more 2D portion gives high separation as seen in Figure 5.11. Figure 5.12 presents the separation when the magnetic fluctuation is varied. We found that low magnetic fluctuation give less separation than the higher one. Similar to the other cases, the particles and the field lines are independent at long time as we can see from slope =1 of the graph.

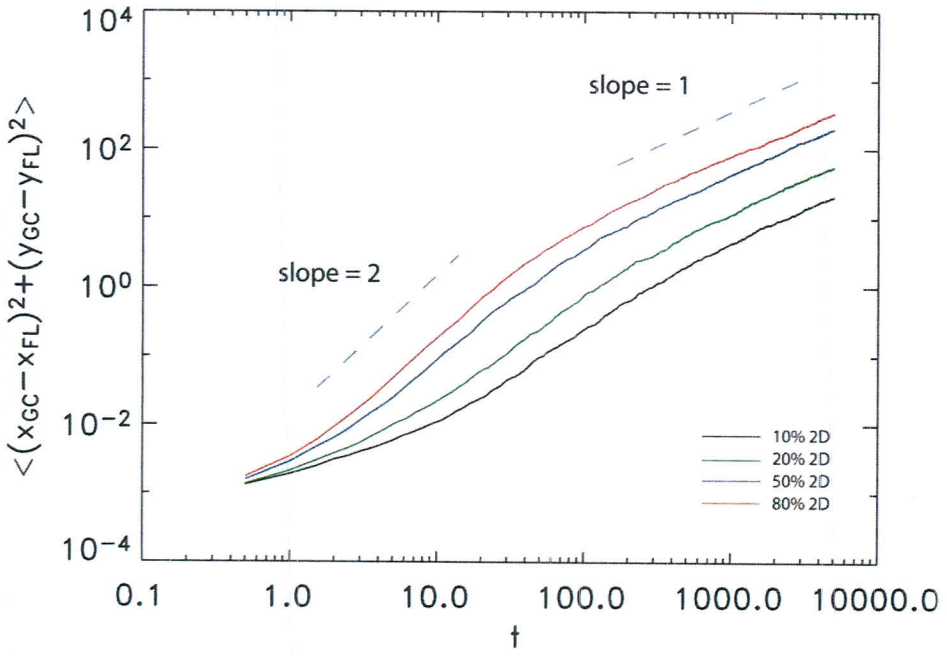

Figure 5.11 The results of the separation of charged particles and their corresponding field lines when we vary particle 2D fraction.

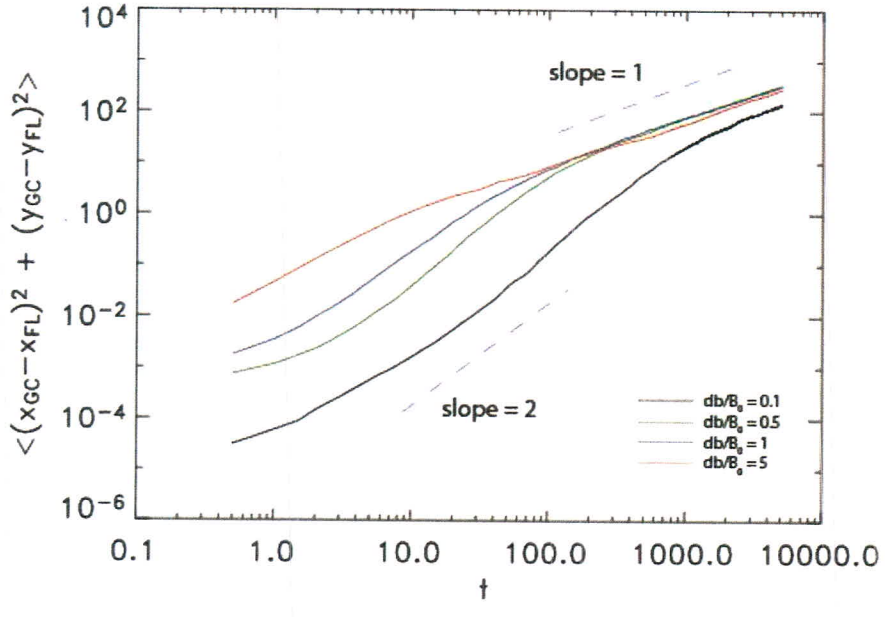

Figure 5.12 The results of the separation of charged particles and their corresponding field lines when we vary magnetic field strength.

In fact, the normalized correlation function and the second order structure functions are related by

$$\hat{R}(\tau) = 1 - \frac{S_2(\tau)}{2\langle F(t)^2 \rangle}. \tag{6.5}$$

Figure 6.1 shows the structure functions for various dissipation range indices q that we generated as described in Sections 2.2 and 3.1.3. Several regimes are seen:

- For $\tau \gg \tau_d$, which is associated with the inertial range ($f^{-5/3}$) in Fourier space, one expects to find $S_2 \propto \tau^{2/3}$.
- For $\tau \ll \tau_d$ and with $q = -5$ and -4, one finds (see Figure 6.1) that $S_2 \propto \tau^2$. This is the regime, in accordance with equation (6.5), in which parabolic curvature of the correlation function is seen near $\tau = 0$.
- For $\tau \ll \tau_d$, but q values of -3 or shallower, the required parabolic behavior is not seen near τ_d, but rather this asymptotic behavior is deferred until $\tau < 1/f_e$. This is due to the fact that the spectrum for this range of q is not steep enough to cause convergence of the Taylor scale estimate. This convergence is now delayed until scales are sampled that are finer than the electron dissipation scale.

This change in behavior of Taylor scale estimates as the dissipation range spectral index is varied is actually very relevant to solar wind observations. For scales smaller than ion inertial length, the solar wind spectral slope is found to be quite variable. For example, Smith et al. (2006b) estimate that dissipation range magnetic spectral indices are broadly distributed with average values $|q| = 2.61 \pm 0.96$ for intervals lacking magnetic clouds, and $|q| = 2.01 \pm 0.84$ for cloud intervals.

A lesson can be learned from the above simple exercise: the asymptotic form of the correlation function embodied in equations (6.2) and (6.5) is not obtained until the sampled spectrum is k^{-4} or steeper. Between spectral indices -4 and -5, the transition to the asymptotic parabolic form migrates towards finer scales, until at k^{-3}, the transition is delayed until separations within the assumed inner cutoff scale are sampled.

From equation (6.5) we can compute the correlation function from the structure function. Figure 6.2 displays the correlation function for various q. From these plots, we can see that the correlation function has a parabolic shape at the origin. At this fixed resolution, the characteristic parabolic shape becomes better defined as the values of $|q|$ are increased.

Suppose now we select a known q and we compute the radius of curvature of the correlation function from data over a range of small separations near the origin $0 < \tau \leq \tau_{fit}$. While this value is intended to be small, to attempt to capture the parabolic regime (if present), the specific value τ_{fit} has no physical significance - it is just a maximum lag to be used in a fitting procedure. This choice of a range of data provides an estimate of τ_{TS}; let us call it $\tau_{TS}^{est}(\tau_{fit})$.

At this point we have obtained an approximate fit, or representation, of the data in this range of τ, given by

$$\hat{R}(\tau) = 1 - \frac{\tau^2}{2\left[\tau_{TS}^{est}(\tau_{fit})\right]^2}. \tag{6.6}$$

This fit is inexact even if the measurements are perfect, because we expect that the Taylor scale is $\tau_{TS} = \lim_{\tau_{fit}\to 0} \tau_{TS}^{est}(\tau_{fit})$. It is not practical to compute this limit because the data has finite time resolution Δt, and because there may be limited data available at the shortest time lags. In another section below we will systematically examine the influence of Δt, the data sampling time.

What can be done however is to compute $\tau_{TS}^{est}(\tau_{fit})$ for a range of τ_{fit}, and to examine the trend of the corresponding values of τ_{TS}^{est} as the maximum lag used in the fit becomes smaller. Figure 6.3 illustrates sequences of such fits $\tau_{TS}^{est}(\tau_{fit})$ versus τ_{fit}. Each of these curves approaches the exact value of Taylor scale in the limit of zero τ_{fit}, as expected. This is for an idealized model times series that can be evaluated at any time separation we wish. Consequently, when a range of τ_{TS}^{est} is available, but only for a set of values of τ_{fit} that excludes the origin, one can try to recover a more precise value of τ_{TS} by an extrapolation technique that provides a refined estimate of the radius of curvature at the origin.

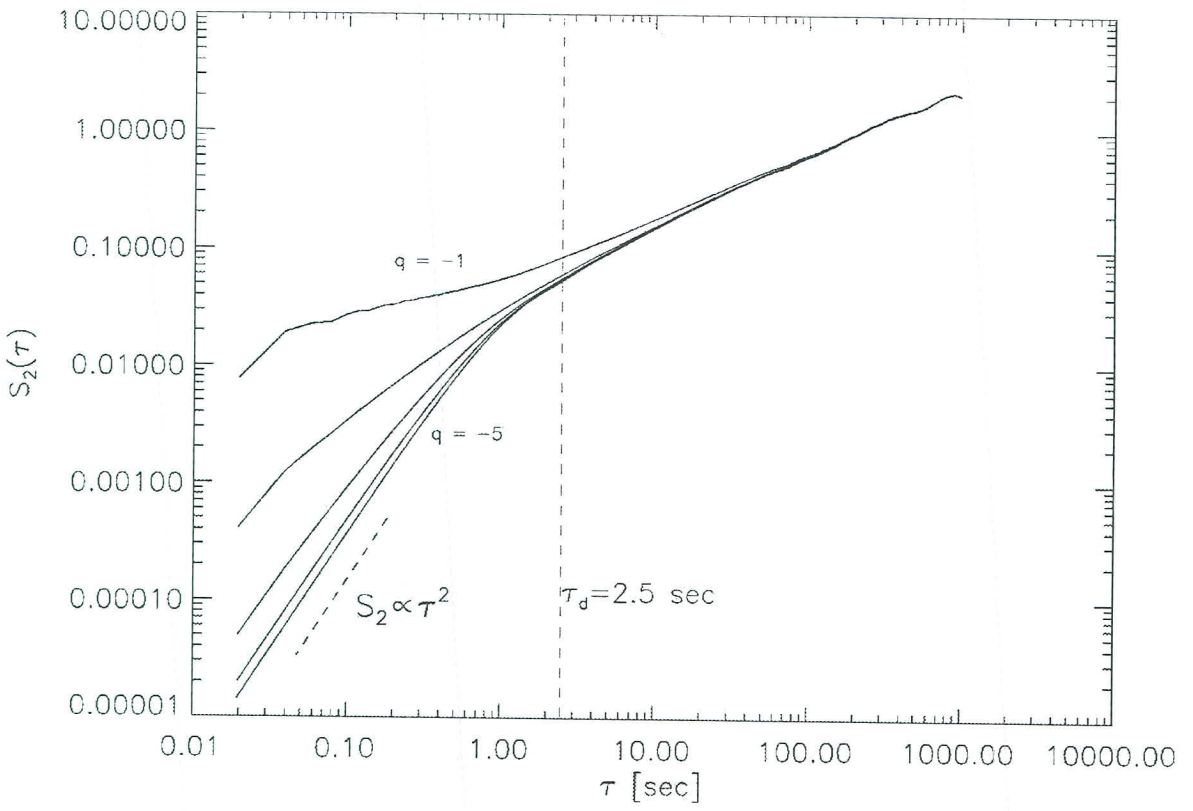

Figure 6.1 The structure function computed from the time series data for a number of values of q. The bottom curve is associated with a q value of -5 and the higher curves are determined with $q = -4, -3, -2$, and -1, respectively.

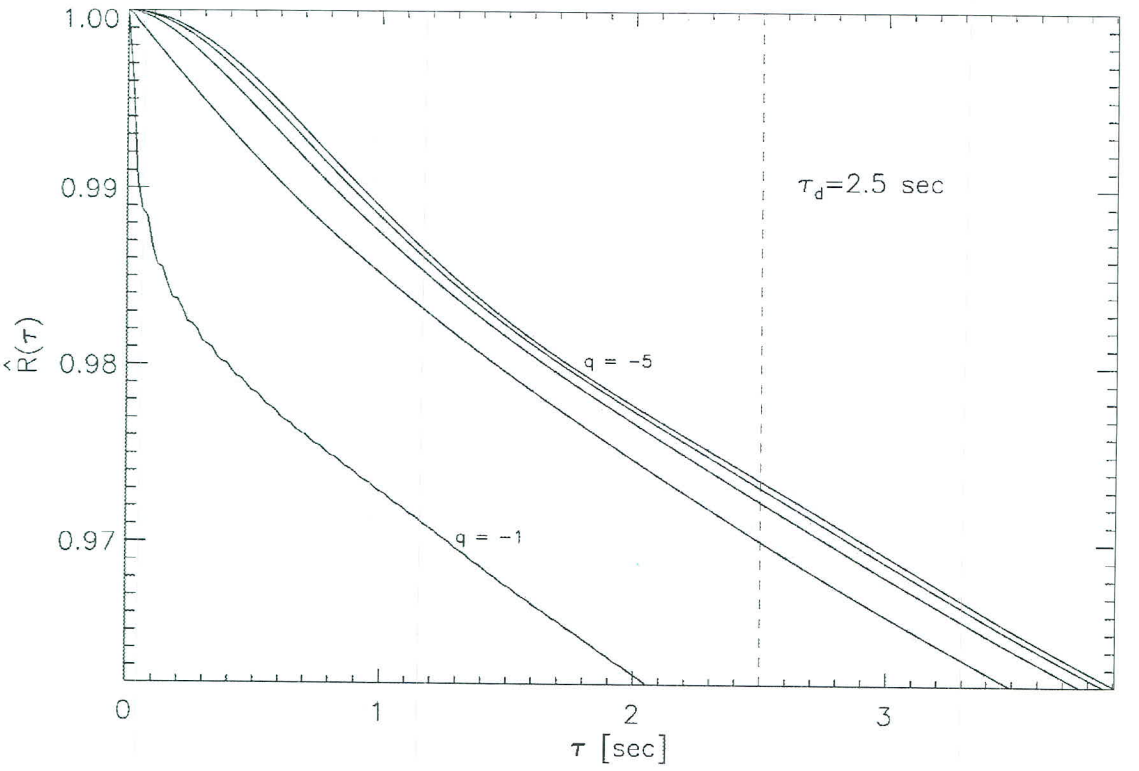

Figure 6.2 The correlation function near the origin. The top curve is determined from $q = -5$ and the next curves are calculated using $q = -4, -3, -2$, and -1, respectively.

6.2 Extrapolation Method

To obtain a stable value for the Taylor microscale at $\tau = 0$, we apply an extrapolation method based on the Richardson extrapolation technique (see Dahlquist and Bjorck, 2003) in analogy with similar procedures employed in numerical analysis. In the first step we compute a series of parabolic fits to data near the origin, and for varying values of τ_{fit}, up to a largest values of τ_{fit}, say, τ_{max}. Using the available estimated values of Taylor microscale $\tau_{TS}^{est}(\tau_{max})$, for this range of τ_{max}, we can compute a straight-line extrapolation of the Taylor scale back to the origin ($\tau_{fit} = 0$). This extrapolation gives a single estimate of a refined value of the Taylor microscale.

Still, it remains unclear which value of τ_{max} we should use. On the one hand; a larger τ_{max} permits the use of more data in the fit process, but a smaller τ_{max} moves us closer to the

asymptotic range in which the formula equation (6.6) for approximating the radius of curvature at the origin becomes more exact.

Therefore we will look for a stable range of values, as follows. Figure 6.4 illustrates the variation of the extrapolated values of Taylor microscale as the value of τ_{max} is varied. In the next step of the method we examine whether for some range of τ_{max} we find a stable value of estimated τ_{TS}^{est}. When working with real data with time cadence Δt, this process is constrained by the temporal resolution, i.e., $\tau_{fit} > \Delta t$. The distribution of number of available estimates at each lag τ can also become an issue. In addition, the quality of the refinement of the Taylor microscale value will depend on the steepness of the spectrum (i.e., q) at the high frequencies.

In the next section we will discuss more details regarding the effects of data resolution and q. For now, (see Figure 6.4) we can make some general statements regarding quality of estimation when a range of estimates is available for time lags near the dissipation (spectral steepening) scale. For large values of q, where the correlation function has a large radius of curvature at the origin (compared to τ_d), we find a value of the Taylor microscale as τ_{max} approaches zero. In contrast, for small values of $|q|$, we do not obtain a stable value of τ_{TS} after the extrapolation.

One can also see by examining Figure 6.4 how lower time resolution data can have an adverse effect. Larger Δt means that the data close to the origin become unavailable for the extrapolation near τ_{fit}=0. The best we might be able to do in such cases is to choose a stable value in the range of $\tau_{max} \sim \tau_d$. By trying this out with the graphs, we see that this approach yields an underestimate of the Taylor microscale value when q is approximately greater than 4 and an overestimate when $|q|$ is approximately less than 4. Our results suggest that a good estimate of τ_{TS} is obtained by a linear extrapolation to zero lag using the slope of the curves τ_{fit}^{est} evaluated near $\tau_{max} = \tau_d$ (see Figure 6.3). In the next subsection we will discuss how we can further improve this estimate with a correction ratio that takes into account known information about the spectra at higher frequencies.

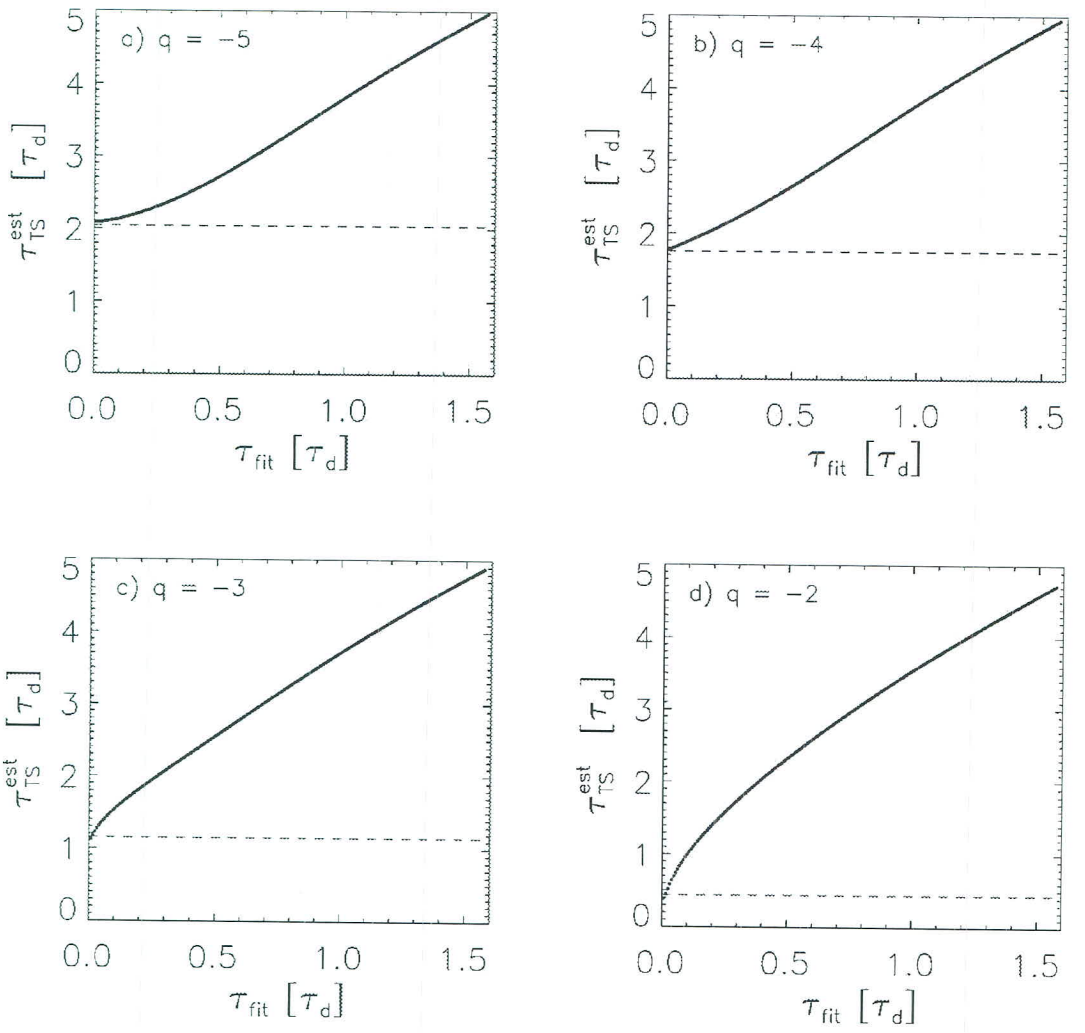

Figure 6.3 Taylor microscale from parabolic fit of the correlation function near the origin for each τ_{fit} for a number of q. Axes are in units of τ_d.

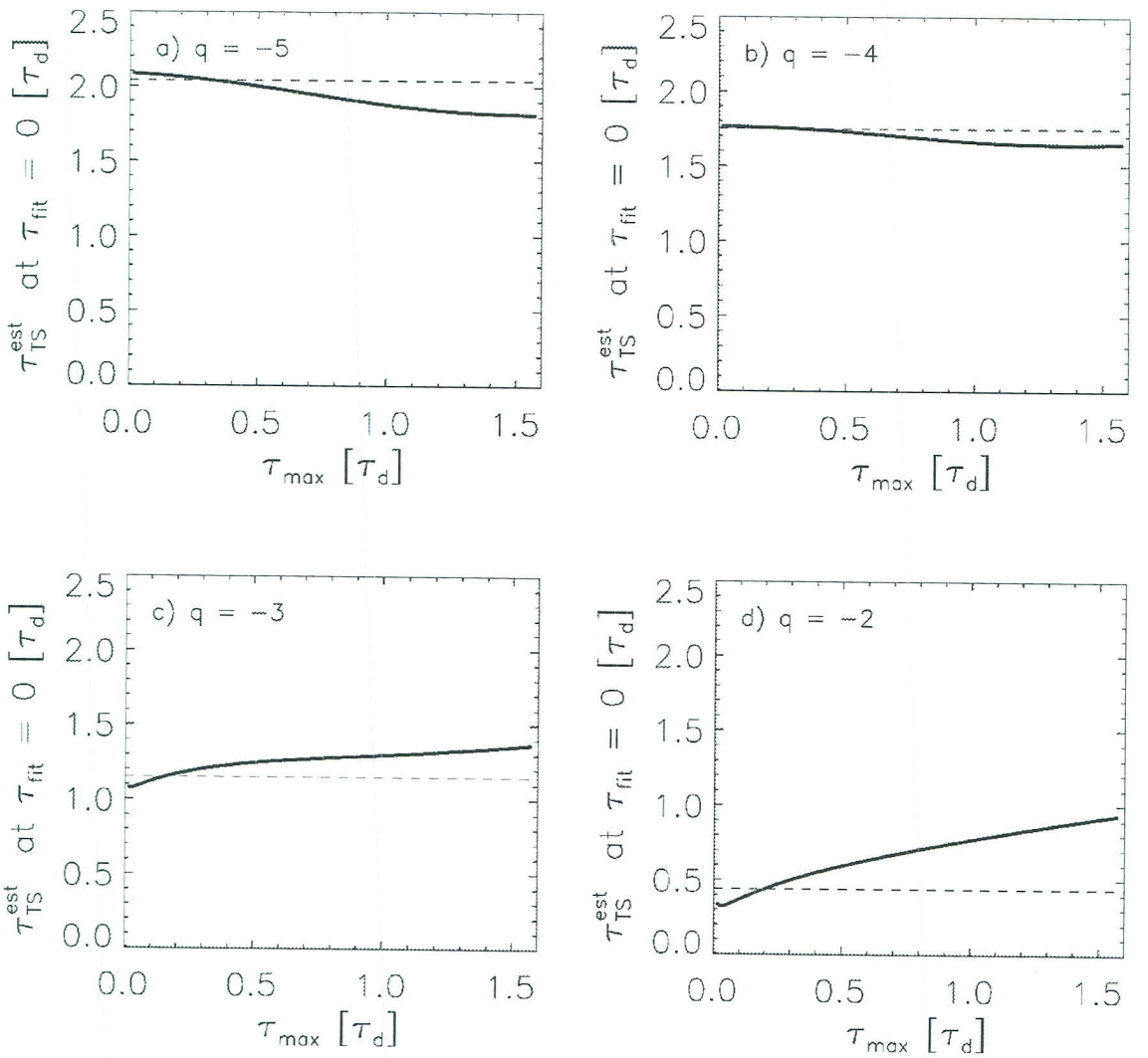

Figure 6.4 Values of τ_{TS} determined by linear extrapolation from the data in Figure 6.3 at the origin (i.e., the intercept). Plotted are the extrapolated Taylor microscale values determined from a range of τ_{max}.

6.3 Correction Ratio

The resolution of the observational data is limited by the instrumentation, the spacecraft data downlink and on board storage. The lower resolution of the data, the less accurate Taylor microscale value will be since it is harder to make measurments that are sensitive to the radius of curvature of the correlation function at the origin. In this section, we examine the effect of the temporal resolution of the data by artificially reducing the resolution of the synthetic time series, and again estimating the Taylor microscale with the same method. The new values for each resolution of the data can be compared with the expected Taylor microscale value to assess the impact of the temporal resolution. In particular, the ratio of these two, ($\tau_{TS}^{expect}/\tau_{TS}$) is of interest. We call this ratio a "correction factor" as it can be employed to estimate the actual Taylor scale given the value computed from finite time resolution data. However this correction must assume knowledge of the spectrum at unresolved frequencies. Here that amounts to knowledge of the value of q.

Figure 6.5 demonstrate the variation of the correction factor when we vary the temporal resolution Δt and the spectral index q. We can see that the correction ratio strongly depends on q. There are three regimes of behavior apparent in the Figure, which we approximate as a piecewise linear function. The model suggested for correction of Taylor scale estimates from finite time resolution data. Accordingly, the empirical correction factor $r(|q|)$ can be written as

$$r(|q|) = \begin{cases} -0.64\left(\frac{1}{|q|}\right) + 0.72, & \text{when } |q| < 2 \\ -2.61\left(\frac{1}{|q|}\right) + 1.70, & \text{when } 2 \leq |q| < 4.5 \\ -0.16\left(\frac{1}{|q|}\right) + 1.16, & \text{when } |q| \geq 4.5. \end{cases} \tag{6.7}$$

With this model for a given data set and a known value of q it is possible to compute a corrected value of the Taylor microscale using

$$\tau_{TS} \approx r(|q|)\tau_{TS}^{extra} \tag{6.8}$$

where τ_{TS}^{extra} is an estimate obtained by the extrapolation method described in Section 6.2 above.

Clearly this procedure presupposes availability of data such that the estimates of Taylor scale are based on near asymptotic tendencies of the functions that are computed. From a practical perspective this appears to require that information about the functions near the dissipation scale τ_d be included in the analysis. Based on the present numerical experiments, we recommend therefore that the resolution of the data be at least as good as $\Delta t < 0.4\tau_d$.

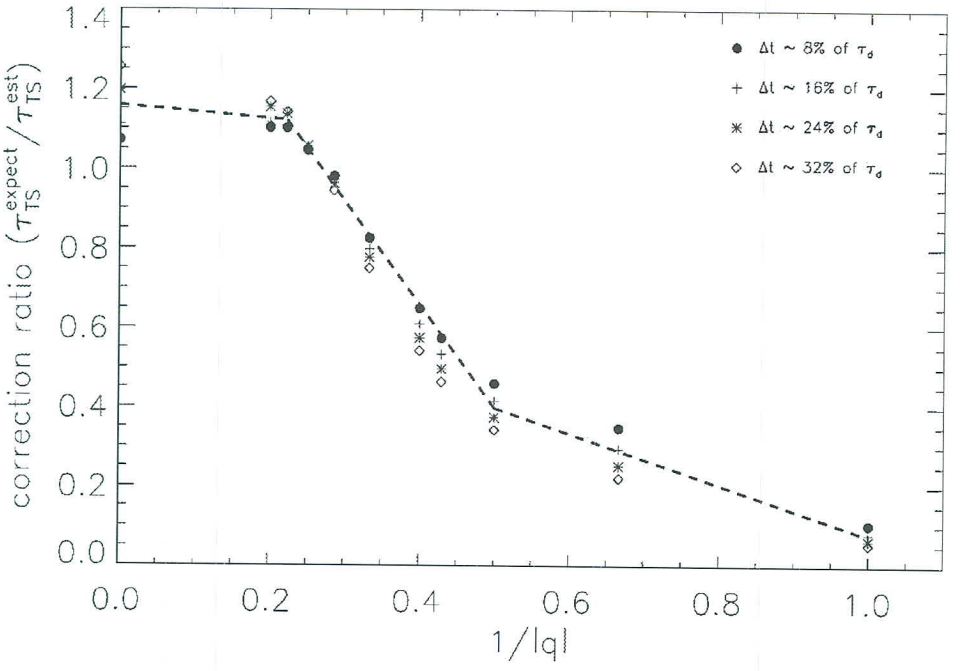

Figure 6.5 Correction ratio versus $1/|q|$ for number of different Δt values.

6.4 Applying the Technique to Spacecraft Data

From an analysis of the magnetic field data from the ACE spacecraft (Smith et al. 2006a), the Taylor microscales in the left column of Figure 6.6 are determined by employing the extrapolation method described above, but without applying the correction ratio. The time resolution of the ACE data used here is $\delta t = 0.333$ s. The black color shows the data from regions characterized as open magnetic field line regions, and the red color shows the data from magnetic clouds (closed field regions). The Taylor scales have already been converted to spatial scales by using frozen-in approximation.

The values obtained for dissipation range spectral index lie between -5 to -1 and the ratio of Taylor scale (λ_T) to the dissipation scale (λ_d) ranges between 0.1 and 10.

The individual plots show that the red and black points appear to be equally scattered. The right column of Figure 6.6 shows the values of λ_T, after the application of the correction ratio. After the corrections, we can see that the majority of the black points have $\lambda_T' > \lambda_d$ for $q < -3$ and the red points have $\lambda_T' < \lambda_d$ for $q > -3$. This indicates a hydrodynamics type of plasma for open magnetic field case and non-hydrodynamics in the magnetic cloud cases. Further discussion of this analysis is found in Matthaeus et al. (2008), where it is argued that the difference in the behavior of these cases points to a difference in relative importance of dissipative processes at ion and electron scales.

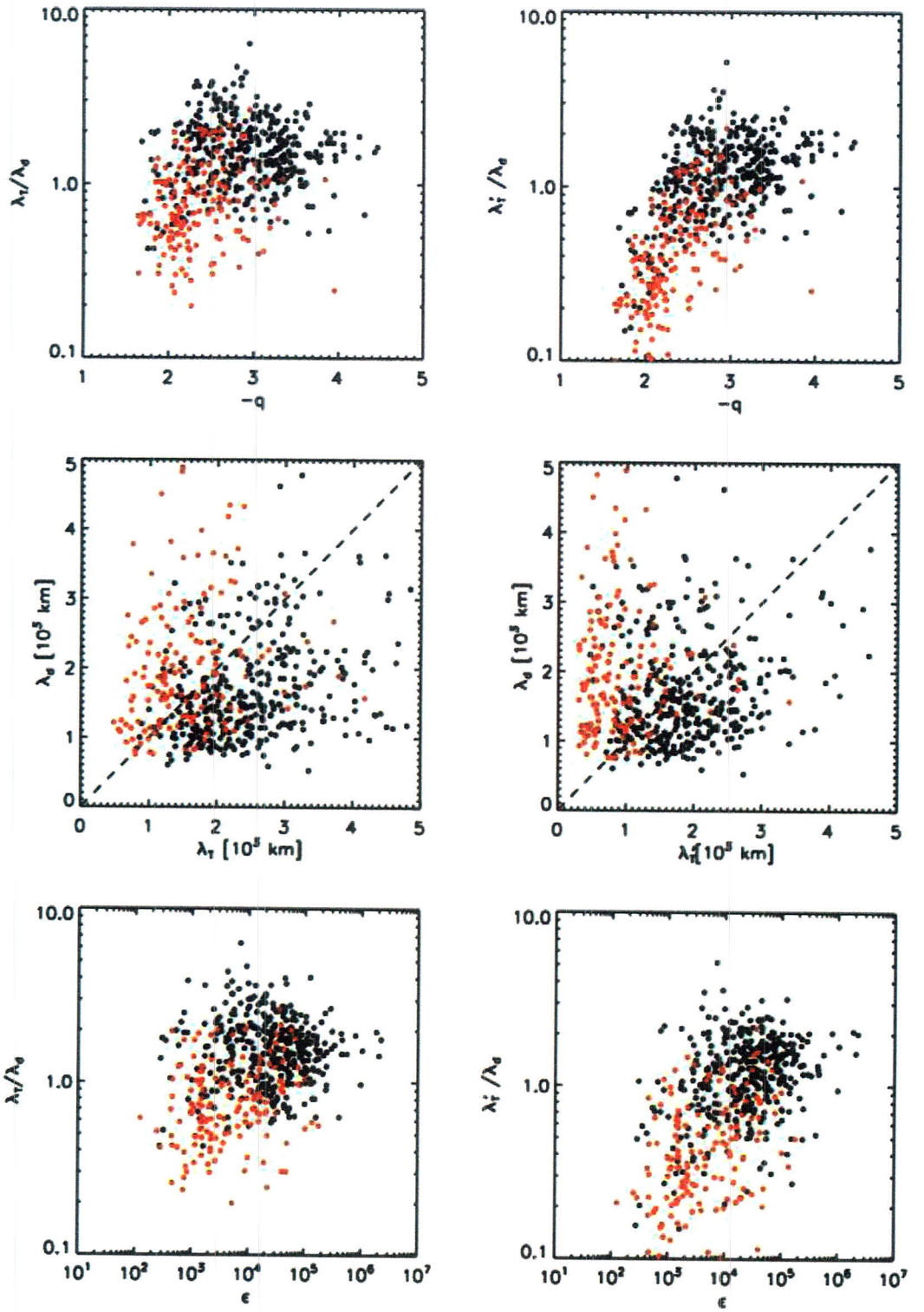

Figure 6.6 The left column shows the plots before applying the correlation ratio to the Taylor mocroscale λ_T and the right column shows the Taylor microscale (λ_T') after applying correlation ratio.

6.5 Conclusions

We have demonstrated a refined technique of calculating the Taylor microscale from a discrete times series by computing correlation functions from structure functions. The method that we employed is based on the definition of the Taylor microscale. To verify this technique we analyze a synthetic time series derived from a defined power density spectrum. We are able to reproduce the Taylor scale values with our technique after applying a correction term, which improves our estimate of the Taylor microscale, estimated from a Richardson extrapolation technique (see Weygand et al. 2009). In addition, we studied the effects of the dissipation range spectral index and the time resolution of the simulated data. Moreover, we show an example of the application of the technique to solar wind magnetic field data (Matthaeus et al. 2005, 2008). This technique is expected to be useful for extracting refined estimates of the Taylor microscale from experimental and observational turbulence data in solar wind and other astrophysical contexts.